Catalysis Science & Technology

Accepted Manuscript

ROYAL SOCIETY OF CHEMISTRY

www.rsc.org/catalysis

Catalysis Science & Technology

ARTICLE

One-step construction of {001} facets-exposed BiOCl hybridized with Al_2O_3 for enhanced molecular oxygen activation†

Received 00th January 20xx,
Accepted 00th January 20xx

DOI: 10.1039/x0xx00000x

www.rsc.org/

Fa-tang Li,*[a] Yi-lei Li,[a] Mei-juan Chai,[a] Bo Li,[b] Ying-juan Hao,[a] Xiao-jing Wang[a] and Rui-hong Liu[a]

{001} Facets-exposed BiOCl with surface oxygen vacancies (SOVs) is developed via a facile ionic liquid (IL) self-combustion route using diethylamine hydrochloride (DLH, $(C_2H_5)_2NH{\cdot}HCl$) as a fuel and a source of the IL cation. It is found for the first time that an excess of DLH can not only facilitate the growth of {001} facets, but also create a reducing atmosphere for combustion, resulting in the release of oxygen atoms on the surface of BiOCl and thus the formation of SOVs. The existence of SOVs lifts the energy band potentials of BiOCl and narrows its energy band gap. To improve the separation efficiency of the photo-generated electrons and holes in BiOCl, amorphous Al_2O_3 is introduced to construct a heterojunction via an in-situ combustion strategy by mixing their aqueous precursors. The heterostructured BiOCl/Al_2O_3 photocatalysts exhibit a noticeable molecular oxygen activation and photocatalytic degradation of rhodamine B. The conduction band (CB) position of amorphous Al_2O_3 is proposed for the first time, which matches well with that of BiOCl with SOVs and contributes to the effective transfer of electrons from BiOCl to Al_2O_3.

Introduction

For nano-catalysts with high specific surface areas, defective surface sites can change their electronic structure and/or physicochemical performance, even at very low concentrations, as well as acting as active sites for adsorption and reaction because of the unsaturated coordination character of surface atoms.[1–3] In the field of photocatalysis, as a fundamental and intrinsic defect, oxygen vacancies play a variety of functions, such as capturing electrons to improve the separation efficiency of charge carriers, narrowing the band gap of a photocatalyst for enhancing visible-light absorption, and enlarging the adsorptive ability for oxygen and/or reactants.[2–10] In addition to surface modification, fabricating a heterojunction is also an effective and widely used method for improving the quantum yield via an enhancement of the charge carriers' transfer.[11] In the most developedtechniques, the two components of hybrids are prepared separately and combined together afterward, which would result in their limited contact interface area and inhibit the efficient transfer of photo-generated electron-hole pairs between them. Because of the different reaction rates and growth processes of crystals related to the nature of the materials, it remains a challenge to prepare heterostructured photocatalysts with a well-contacted structure by a one-pot facile strategy.[12]

Meanwhile, seeking cheap and Earth-abundant materials is indispensable to achieving industrial production.[13] Aluminium is the most abundant metal element in Earth's crust, which makes Al_2O_3 very inexpensive, green, sustainable, and combined with its nontoxicity, results in the prospect for a wide range of applications. Therefore, Al_2O_3 has been extensively used as a support in the areas of catalysis and materials. For a long time, Al_2O_3 has beenapplied as an inert support for photocatalysts to adjust their surface areas, porous structures, dispersion performance, adsorptivity for reactants, or stability.[14–18] Recently, Hankare et al.[19] reported the active role of Al_2O_3 in accepting photo-induced electrons from other contacted photocatalysts. Our group further found that amorphous Al_2O_3 has an ultraviolet-light-responsible ability and attributed it to the shorter length of the Al-O bond on the basis of Ishimaru's calculation that the Al-O bond length in amorphous $MgAl_2O_4$ is smaller than that in the normal spinel structure.[20–22] We have also constructed effectively amorphous α- or γ-Al_2O_3-based photocatalysts.[20,23–25] Recently, more researchers confirmed the photoactive role in the acceptance electrons by defective Al_2O_3.[26,27] However, the energy band position of the Al_2O_3 defects has not been reported, which is an important parameter for guiding the construction of heterojunctions and broadening the application of inexpensive Al_2O_3 in fields concerning energy and environment.

In recent years, bismuth oxyhalide compounds BiOX (X=F, Cl, Br, or I) have attracted tremendous research interest because of their efficient photocatalytic ability for environment remediation and energy conversion, which originates from their unique layered tetragonal structure.[28–32] In the BiOX family, BiOCl exhibits superior photocatalytic reduction and oxidation performance; however, its wide

[a] College of Science, Hebei University of Science and Technology, Shijiazhuang 050021, China.
Email: lifatang@126.com
[b] Analytical and Testing Centre of Hebei Province, Hebei University of Science and Technology, Shijiazhuang 050021, China.
† Electronic supplementary information (ESI) available. See DOI: 10.1039/

energy band gap (ca. 3.2-3.4 eV) and relatively low quantum yield restricts its practical application for solar light. The fabrication of oxygen vacancies on the surface of BiOCl to expand its optical absorption from UV to visible light and the construction of heterojunctions to enhance the separation efficiency of photo-generated electron-hole pairs have attracted significant attention.[10,32–34] However, to our knowledge, the synchronous fabrication of surface oxygen vacancy on BiOX and hybridization with inexpensive materials has not been reported.

In this work, we firstly constructed BiOCl with surface oxygen vacancies (SOVs) via a ionic liquid self-combustion route and then one-step synthesized $BiOCl/Al_2O_3$ heterojunctions for activating molecular oxygen (O_2), which is a green and effective oxidant for various oxidative reactions.[33,35,36] The used ionic liquid self-combustion was proposed by our group,[37] which not only is a time- and energy-technique, but can also ensure thehomogeneous mixing of the precursors at a molecular level, which facilitates the formation of heterojunctions with more contact sites and the transfer of charge carriers between the components.[38] Via self-combustion, SOVs were successfully self-constructed on the as-prepared BiOCl, which exhibitsa visible-light-response ability and a raised conduction band (CB) potential. Based on the formation of BiOCl with SOVs, $BiOCl/Al_2O_3$ hybrids were in-situ fabricated yielding an enhanced performance for O_2 activation. Meanwhile, the CB position of the defective Al_2O_3 obtained via solution combustion is presented for the first time.

Experimental Section

Chemicals and catalysts preparation

All chemicals were purchased from Sinopharm (Shanghai, China) and used as received without further purification. For synthesizing BiOCl with SOVs, 0.005 mol $Bi(NO_3)_3{\cdot}5H_2O$ was mixed with 0.007 mol diethylamine hydrochloride (DLH, $(C_2H_5)_2NH{\cdot}HCl$), and then the mixture was heated on an electric furnace until the formation of a white solution, which is an ionic liquid (IL, $[(C_2H_5)_2NH{\cdot}H]^+[Bi(NO_3)_3Cl]^-$).[39] Afterwards, the IL was moved into a tube furnace and heated at 300 °C for 3 min at a heating rate of 10 °C min^{-1} and a O_2 flow rate of 500 mL min^{-1}. Finally, the BiOCl with SOVs were obtained and labelled as BiOCl-S. For comparison, the BiOCl without SOVs was prepared using 0.005 mol $Bi(NO_3)_3{\cdot}5H_2O$ and 0.005 mol DLH, which is named BiOCl-C.

To acquire the $BiOCl/Al_2O_3$ hybrids, $Al(NO_3)_3{\cdot}9H_2O$ was synchronously added to the mixture of $Bi(NO_3)_3{\cdot}5H_2O$ and DLH. The designed various ratios of $BiOCl/Al_2O_3$ are listed in Table 1, which are denoted as XBA (X represents the molar ratio of BiOCl to Al_2O_3). The molar ratio of fuel to nitrates was kept at 1.4.

Material characterization and analysis

X-ray diffraction (XRD) analysis was carried out on a Rigaku D/MAX 2500 X-ray diffractometer. The morphology and the elemental distribution of the as-prepared samples were observed by means of a field-emission scanning electron microscope (FE-SEM) and element mapping images from a Hitachi S4800 instrument equipped with an energy dispersive X-ray spectrometer (EDS, Bruker Quantax). High-resolution transmission electron microscopy (HRTEM) images were acquired by a JEOL JEM-2010 electron microscope. The photo-absorption properties of the photocatalysts were evaluated by UV–Vis diffuse reflectance spectra (DRS) with a Thermo Scientific Evolution 220 spectrophotometer. N_2 adsorption/desorption measurements were carried out on Micromeritics Tristar II 3020 apparatus. The surface charges of the samples were acquired by a Zeta-potential analyser (Horiba SZ-100-Z) after ultrasonic dispersing 0.1 g of sample powders in 100 mL of deionized water for 10 min. Time-resolved photoluminescence (PL) spectroscopy was recorded on an FS5 Fluorescence spectrometer (Edinburgh Instruments) with an excitation source at 310 nm. The photocurrent measurements were carried out on a CHI 660E electrochemical workstation (Shanghai, China) using a standard three-electrode quartzcell under an applied bias of 0.5 V. The photocatalyst films deposited on clean 1.5 cm × 1.0 cm fluoride-tin oxide (FTO) glass were prepared as working electrodes. The reference and counter the electrodes were Ag/AgCl (saturated KCl) and platinum wire, respectively. 0.5 M Na_2SO_4 was employed as the electrolyte solution. Mott-Schottky plots were obtained to evaluate the energy band positions of the photocatalysts at a frequency of 1 kHz using a CHI 660E electrochemical workstation in the dark. Electrochemical impedance spectroscopy (EIS) was carried out at the open-circuit potential and recorded over a frequency range of 1 to 1×10^5 Hz with an ac amplitude of 5 mV. Electron spin resonance (ESR) spectra were collected using a Bruker EMX-8/2.7 X-band ESR spectrometer to observe the oxygen vacancies of the powders.

Table 1. Designed sample compositions from different amounts of raw materials.

Sample	$Bi(NO_3)_3$(mol)	DLH(mol)	$Al(NO_3)_3$(mol)	n(BiOCl:Al_2O_3)
BiOCl-S	0.0050	0.0070	0	1:0
BiOCl-C	0.0050	0.0050	0	1:0
Al_2O_3	0	0.0140	0.010	0:1
0.6BA	0.0030	0.0182	0.010	0.6:1
0.8BA	0.0040	0.0196	0.010	0.8:1
1.0BA	0.0050	0.0210	0.010	1.0:1
1.2BA	0.0060	0.0224	0.010	1.2:1
1.4BA	0.0070	0.0238	0.010	1.4:1

Oxygen activation and photocatalytic activities test

The superoxide anion radical ($\bullet O_2^-$) is a main product of molecular oxygen after activation. To determine the O_2 activation performance, p-nitro blue tetrazolium chloride (NBT, 2.5×10^{-5} mol/L) was used as an indicator of $\bullet O_2^-$; NBT has a maximum absorption wavelength of 260 nm, while the adduct of $\bullet O_2^-$ and NBTdoes not.[40,41] The degradation experiment of NBT was conducted as follows: after dissolving NBT in H_2O to form a 2.5×10^{-5} mol/L solution, 0.10 g of photocatalyst was put into 100 mL of the NBT solution and then irradiated under visible light. A 350-W Xe lamp equipped with a 400 nm cut-off filter served as the visible light source. At a given interval, 5mL of the aqueous solution was sampled,

centrifuged, and filtered to remove the photocatalyst powders and then measured on a Thermo Scientific Evolution 220 spectrophotometer. The relative concentration of the hydroxyl radical (•OH), a general radical generated in the photocatalytic process, was estimated using a terephthalic acid (TA) fluorescence technique based on the fact that TA can react with •OH radicals to form the highly fluorescent 2-hydroxyterephthalic acid (TAOH), the signal of which can be recorded on a fluorescence spectrophotometer.[42,43] To perform this experiments, TA was firstly dissolved in 2.0 mM NaOH to obtain a 0.5 mM TA solution. Afterwards, 0.1 g of the photocatalyst was dispersed in 100 mL of the solution. After being irradiated with visible light, the fluorescence spectra were recorded on a Hitachi F-4600 fluorescence spectrophotometer (excitation wavelength: 315 nm). In addition, the ESR signals of the radicals spin-trapped by 5,5-dimethyl-l-pyrroline-N-oxide (DMPO) were collected under visible-light irradiation (λ>400 nm) to directly observe the existence of $\bullet O_2^-$ or •OH radicals.

The photocatalytic activity of the samples was also evaluated by the decomposition of rhodamine B (RhB, 10 mg/L) and phenol (50 mg/L). The photocatalyst (0.10 g) was mixed with 100 mL of the pollutant solution. Prior to illumination, the suspension was magnetically stirred in darkness for 0.5h to reach the adsorption/desorption equilibrium. During the photocatalytic process, 2 mL of the suspension was taken at fixed intervals and centrifuged to measure the concentration of pollutants using a Thermo Scientific Evolution 220 UV-vis spectrophotometer at their maximum absorption wavelength. Because of the continuous evaporation of water during the irradiation (about 5 mL reduction of 100 mL in 1 h reaction), the corresponding water was added to the solution before sampling for precise absorbance measurement. To detect the active species responsible for the degradation of RhB, various scavengers, including isopropanol (IPA, 10 m mol/L, •OH scavenger[44]), 1,4-benzoquinone (BQ, 1 mM, $\bullet O_2^-$ scavenger[45]), and ethylenediamine tetraacetic acid disodium salt (EDTA-2Na, 10 mmol/L, hole scavenger[46]) were employed in the photocatalytic degradation of RhB.

Results and discussion

Formation and characterization of BiOCl with surface oxygen vacancies

Fig. 1a shows the XRD patterns of BiOCl-S and BiOCl-C, which were obtained with different amounts of DLH fuel. Both of the samples exhibit peaks consistent with the standard BiOCl phase (JCPDS NO. 01-082-0485) without observing any other peaks from possible intermediates and undecomposed raw materials, indicating the excellent combustion conditions for forming BiOCl. Meanwhile, it should be noted that the (001) peak of BiOCl-S is clearly stronger than other peaks, while in the cases of BiOCl-C and standard BiOCl, the peak corresponding to the (101) plane is the highest one. The quantitative intensity ratios of the (001) versus (101) peaks for different samples are presented in Fig. 1b, which are 0.677, 1.310, and 0.714 for the referenced standard BiOCl, BiOCl-S,

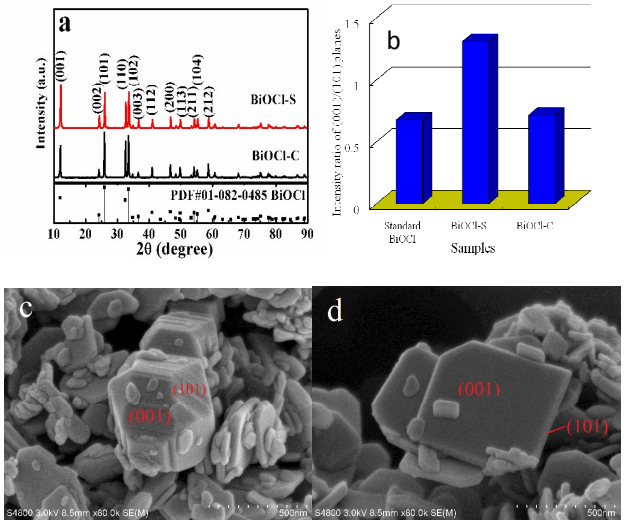

Fig. 1. (a) XRD patterns of the as-prepared samples, (b) the intensity ratiosof (001)/(101) peaks for BiOCl-S, BiOCl-C, and the BiOCl referenced standard, and SEM images of (c) BiOCl-C and (d) BiOCl-S.

and BiOCl-C. This phenomenon indicates that DLH, as a fuel for the combustion synthesis of BiOCl-S and BiOCl-C, can induce the growth of the crystal along the direction of the (001) plane.

To directly observe their morphology concerning the planes, SEM images of BiOCl-C and BiOCl-S were collected as shown in Fig. 1c and d. It is obvious that BiOCl-S exhibits thinner flake-like structure with higher (001) plane ratio than BiOCl-C.

Thus, both BiOCl-S and BiOCl-C have higher intensity ratios in (001)/(101) peaks than the referenced BiOCl, and BiOCl-S prepared with more DLH has the highest ratio of 1.310. Because BiOX is thought to possess a higher separation efficiency of photo-generated electrons and holes along the (001) direction than any other directions according to the experimental results and theoretical calculations,[28,47,48] the exposed {001} facets of the as-prepared BiOCl-S would facilitate the enhancement of photocatalytic activity.

To further analyse the difference between BiOCl-S and BiOCl-C, both of their potential combustion reactions are firstly proposed according to the propellant theory.[38,49]

$$Bi(NO_3)_3 \cdot 5H_2O + 1.4(C_2H_5)_2NH \cdot HCl + 5.7O_2 \rightarrow BiOCl - S + 5.6CO_2 + 2.2N_2 + 13.2H_2O + 0.4HCl \quad (1)$$

$$Bi(NO_3)_3 \cdot 5H_2O + 1.0(C_2H_5)_2NH \cdot HCl + 3.0O_2 \rightarrow BiOCl - C + 4.0CO_2 + 2.0N_2 + 6H_2O \quad (2)$$

It is observed that the formation of BiOCl-S requires more oxygen to accomplish the combustion reaction. In other words, a combustion condition of excess DLH added to the system would lead to a reducing atmosphere when the supplied oxygen flow is not sufficient.[50] It is known that the oxygen in the whole system should maintain an equilibrium

between species in the atmosphere and species in the crystal lattice. Hence, in a reducing atmosphere, oxygen atoms would escape

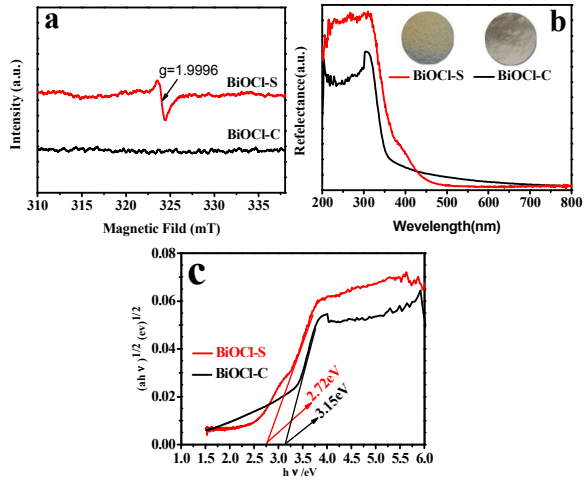

Fig. 2. (a) ESR spectra, (b) UV-vis DRS, and (c) aplot of $(\alpha h\nu)^{1/2}$ versus $h\nu$ for BiOCl-S and BiOCl-C.

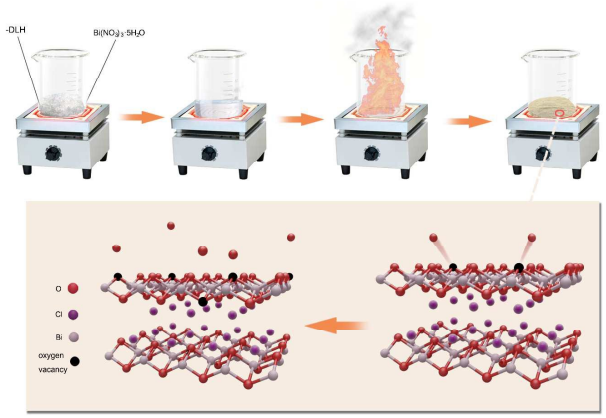

Scheme 1. Schematic formation route of surface oxygen vacancies in BiOCl during the combustion process.

from the surface of the BiOCl lattice to the atmosphere, leaving oxygen vacancies. The process can be expressed by the following equation using Kroger-Vink notation.[6]

$$O_O = V_O^{\bullet\bullet} + 1/2O_2(g) + 2e' \quad (3)$$

To verify the above hypothesis, some characterizations were carried out. Firstly, a clear ESR signal from sample BiOCl-S at g = 1.9996 is found, as shown in Fig. 2a, which is derived from the superoxide ion generated by atmospheric oxygen adsorbed at the surface oxygen vacancy.[7] In contrast, no clear signal can be detected for BiOCl-C. Therefore, this indicates that combustion via only adjusting the fuel amount is a convenient and efficient strategy for the preparation of BiOCl with surface oxygen vacancies.

It is known that oxygen vacancies reduce the band gap of the photocatalyst, which can be detected by UV-vis DRS. As shown in Fig. 2b, there is a clear red-shift for BiOCl-S compared with BiOCl-C, which is consistent with their appearance (yellow for BiOCl-S and white for BiOCl-C). The detailed band gap

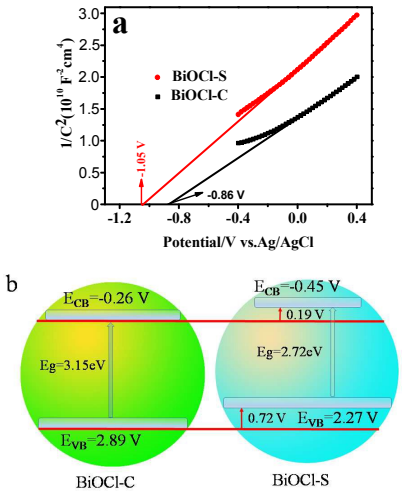

Fig. 3. (a) Mott–Schottky plots measured in a 0.5 M Na_2SO_4 solution, and (b) the proposed energy band potentials of BiOCl-S and BiOCl-C.

energies of both of the semiconductors are evaluated by the following equation:[51]

$$\alpha(h\nu) = A(h\nu - Eg)^{n/2} \quad (4)$$

where α, h, ν, A, and E_g are the absorption coefficient, Planck's constant, light frequency, energy-independent constant, and band gap, respectively. For BiOCl, n is 4 because of its indirect transition. According to the equation, the band gaps of the samples are obtained by extrapolating the tangent lines to $(\alpha(h\nu))^{1/2}=0$, as shown in Fig. 2c, and are 3.15 and 2.72 eV for BiOCl-C and BiOCl-S, respectively. These values correspond to absorption wavelength thresholds of 393 and 456 nm, indicating the existence of oxygen vacancies in BiOCl-S.

On the basis of the combustion process and the fact of the SOVs existence, a potential formation route for SOVs is proposed in Scheme 1.

To elucidate the influence of oxygen vacancies on the electronic structure, a Mott–Schottky test was employed for obtaining the relative band positions of BiOCl with and without oxygen vacancies. Generally, the flat-band potential values of electrodes are determined by the following Mott–Schottky equation:[53]

$$\frac{1}{C_{SC}^2} = \frac{2}{e\varepsilon\varepsilon_0 N_d}(V_a - V_{fb} - kT/e) \quad (5)$$

where C_{sc} is the space charge capacitance in F cm^{-2}, e is the electronic charge in C, ε is the dielectric constant of the semiconductor, ε_0 is the permittivity of vacuum, N_D is the carrier density in cm^{-3}, k is the Boltzmann constant, T is the temperature in K, V_a and V_{fb} are the applied potential and the flat band potential in V, respectively. The flat band potential

can be deduced from the x-intercept of the tangent line of the $1/C^2$ plots with the potential axis.

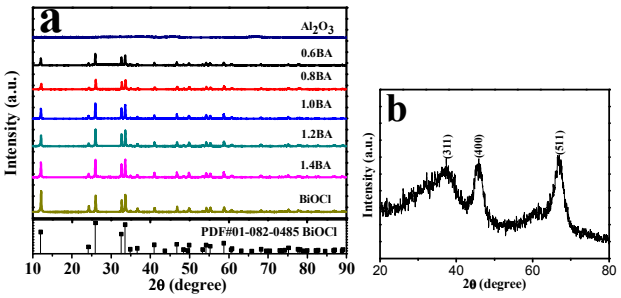

Fig. 4. (a) XRD patterns of the as-prepared samples and (b) a magnification of the XRD pattern of Al_2O_3.

As shown in Fig. 3a, the positive slope of the Mott–Schottky plots demonstrates the n-type characteristic of both as-prepared BiOCl materials.[53] It is also observed that the obtained V_{fb} for the BiOCl-S and BiOCl-C electrodes are −1.05 and−0.86 V (versus Ag/AgCl), respectively, which can be converted to the reversible hydrogen electrode (RHE) scale by the following relation, $E_{RHE}=E_{(Ag/AgCl)}+0.6$ V.[54,55] Thus, the flat band potentials of BiOCl-S and BiOCl-C are -0.45 and -0.26 V *vs*. RHE, respectively. RHE corresponds to the standard hydrogen electrode (SHE) at pH=0. Furthermore, it is believed that the flat band potential is close to the conduction band (CB) position in an n-type semiconductor.[56] That is, BiOCl-S and BiOCl-C display CB minimums at -0.45 and -0.26 V, respectively. According to the measured energy band gaps, the valence band (VB) maximum energies of BiOCl-S and BiOCl-C, are 2.27 and 2.89 eV, respectively. The energy band positions are shown in Fig. 3b.

For the BiOCl-S photocatalyst with surface oxygen vacancies, the VB maximum up-shifts by 0.72 V compared with that of BiOCl-C without oxygen vacancies. Meanwhile, the CB minimum of BiOCl-S up-shifts by 0.19 V compared with that of BiOCl-C. From the point of view of kinetic and thermodynamic research on the separation of the carriers and the generation of radicals, two features—the VB width and the CB minimum energy—should be noticed:[10] firstly, the increased VB width is helpful for the separation of the photo-induced electrons and holes because the wider the VB width is, the higher the mobility of the photo-generated holes becomes. Secondly, the lift of the CB minimum benefits the reaction between the photo-induced electrons and molecular oxygen adsorbed on the surface of catalyst to form more superoxide anion radicals accelerating the photocatalytic reaction.

Structure and morphology of BiOCl/Al_2O_3 heterojunctions

Fig. 4a shows the XRD patterns of the as-prepared pure BiOCl, Al_2O_3, and the BiOCl/Al_2O_3 composites. For BiOCl and the BiOCl/Al_2O_3 composites, the peaks are consistent with the tetragonal BiOCl phase (JCPDS No. 01-082-0485). With a decrease in the BiOCl content, the peak intensity becomes weak. Meanwhile, there are no obvious Al_2O_3 peaks that can be observedin the composites, even in the pure Al_2O_3 pattern. To observe the crystal phase of Al_2O_3 clearly, a magnification of the XRD pattern is shown in Fig. 4b. It can be observed from

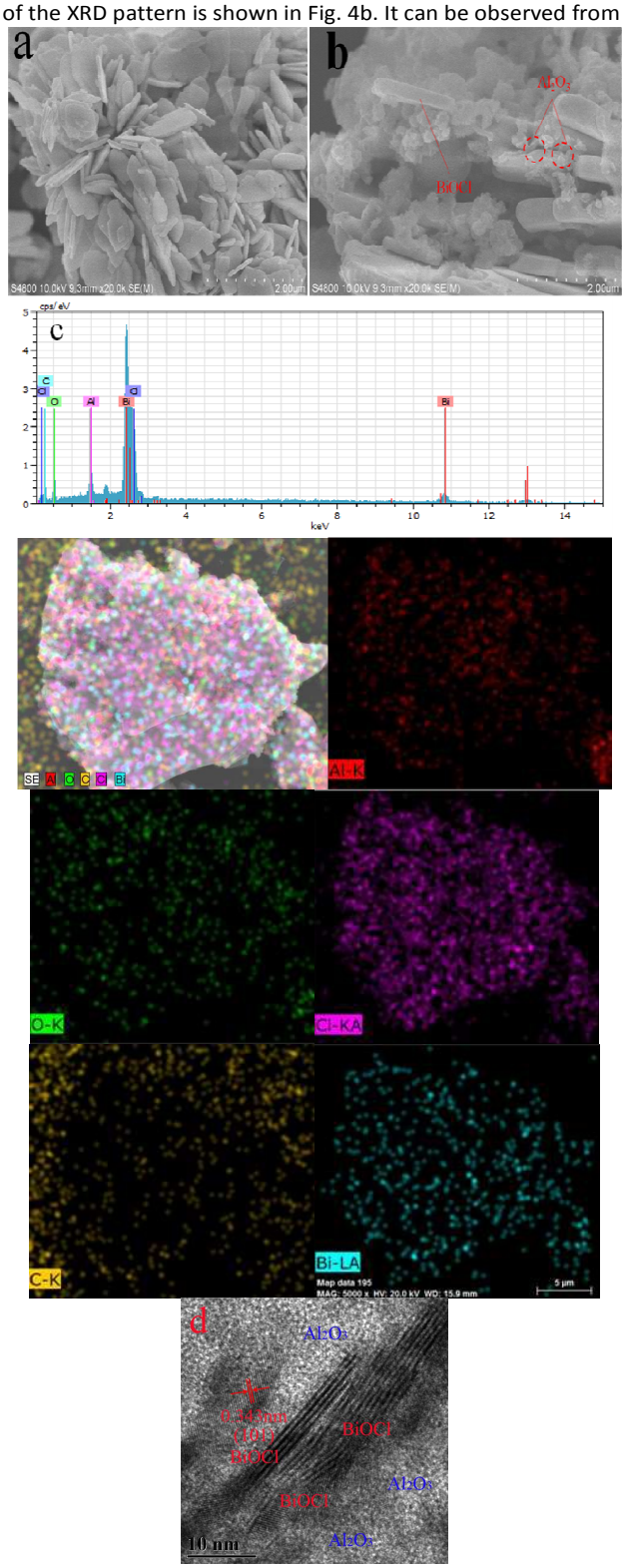

Fig. 5. SEM images of (a) the pure BiOCl-S and (b) 1.0BA; (c) the EDS spectrum and the corresponding elemental mapping images of 1.0BA; and (d) HRTEM images of 1.0BA.

Fig. 4b that there are mainly three peaks at 37.4°, 45.5° and 66.9° corresponding to the (311), (400) and (440) diffraction planes of cubic γ-Al_2O_3 (JCPDS No. 10-0425); furthermore, the broad peaks suggest a low crystallinity and the existence of defect sites, which is beneficial for accepting photo-induced electrons from other components of the hybrid.[19,22,23] Other peaks from the raw materials of $Al(NO_3)_3$ and DLH cannot be detected, implying the combustion of $Al(NO_3)_3$ in the presence of DLH for the synthesis of Al_2O_3 is complete. The reaction equation can be expressed as follows, in which the requirement for oxygen is similar to that in the formation of BiOCl-S.

$$Al(NO_3)_3 \cdot 9H_2O + 1.4(C_2H_5)_2NH \cdot HCl + 5.95O_2 \rightarrow 0.5Al_2O_3 + 5.6CO_2 + 2.2N_2 + 17.2H_2O + 0.4HCl \quad (6)$$

The morphology and interface structure were observed by scanning electron microscopy (SEM) and high-resolution transmission electron microscopy (HRTEM). As shown in Fig. 5a, the pristine BiOCl exhibits a typical nanosheet-like characteristic, which is in accordance with the observed morphology of previous reports.[32,33,39] From Fig. 5b, it is seen that the Al_2O_3 particles adhereto the surface of BiOCl in the case of the 1.0BA sample, illustrating their heterostructure. In addition, the EDS test shown in Fig. 5c and the corresponding elemental mapping pictures clearly indicate the co-existence of Bi, O, Cl, and Al elements in 1.0BA, offering direct visual evidence for the combination of BiOCl and Al_2O_3. Fig. 5d shows the HRTEM image of the 1.0BA composite. It is apparent that there are two types of areas. One is composed of a lattice fringe, in which the interplanar spacing is approximately 0.343 nm. This value corresponds to the (101) plane of BiOCl. The other region consists of cloud-like materials without a lattice fringe, which implies its amorphous-similar structure and is in agreement with the XRD result.

Oxygen activation and photocatalytic performance of the photocatalysts

In photocatalysis, the main route for activating oxygen is the reaction between oxygen molecules and electrons to generate $\bullet O_2^-$. The amount of $\bullet O_2^-$ produced in the process is a measure of the oxygen activation ability of the photocatalysts. The NBT test method is widely used to quantitatively compare the amount of $\bullet O_2^-$. Fig. 6a demonstrates the variation of the degree of NBT degradation (C/C_0) with time under visible-light irradiation. It is obvious that the 1.0BA exhibits the highest degradation ability for NBT, that is, the strongest oxygen activation performance. The photocatalytic oxygen activation availability is evaluated by the reaction rate constant listed in the following the Langmuir–Hinshelwood pseudo-first-order kinetics equation, which can be used in the degradation of pollutants with low initial concentrations:[20]

$$\ln C_0 / C_t = kt + \ln C_0 / C_1 \quad (7)$$

where k is the rate constant, C_0 is the initial concentration of NBT (10 mg/L), C_1 is the concentration after adsorption, and C_t is the concentration at reaction time t. In this case, the adsorption of NBT on the catalysts can be ignored and the equation is simplified as follows:

$$\ln C_0 / C_t = kt \quad (8)$$

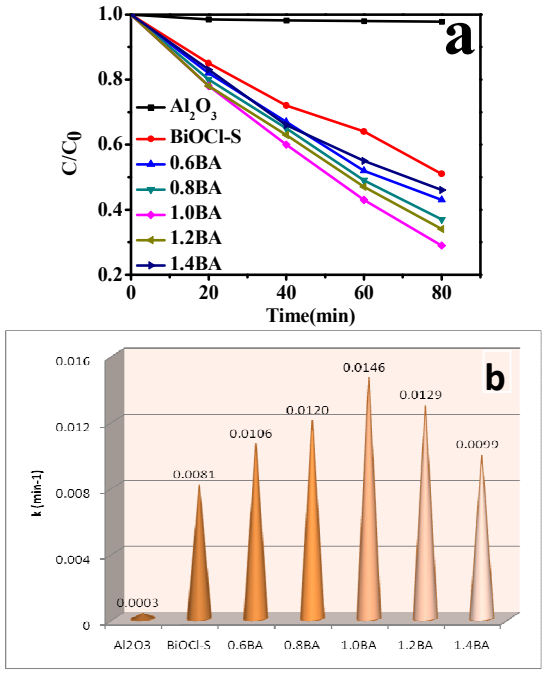

Fig. 6. (a) Time-course variation of C/C_0 of NBT under visible-light illumination, and (b) the corresponding reaction rate constants(k)for various samples.

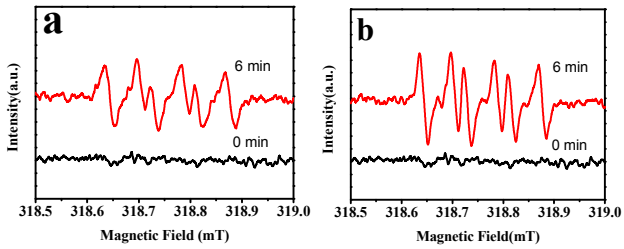

Fig. 7. DMPO-$\bullet O_2^-$ spin-trapping ESR spectra for (a) BiOCl-S and (b) 1.0BA without and with visible-light irradiation.

The reaction rate constants (k) fitted from the plots of C/C_0 areshown in Fig. 6b, from which it is clear that the sample of 1.0BA has the highest rate constant. The k value of 1.0BA is 1.80 times that of the sample of pristine BiOCl; meanwhile, all of the heterostructured photocatalysts have higher k values than that of the BiOCl, exhibiting their enhanced oxygen activation performance and indicating the in-situ construction of BiOCl/Al_2O_3 is an efficient strategy for activating oxygen molecules.

The ESR results are shown in Fig. 7 and directly reveal the existence of $\bullet O_2^-$. There is no DMPO-$\bullet O_2^-$ adduct peak without light irradiation. After 6 min of illumination, both BiOCl-S and 1.0BA exhibit obvious signals of the DMPO-$\bullet O_2^-$ adduct,

implying the generation of $\bullet O_2^-$ radical species in the presence of the photocatalysts and visible-light. In addition, the sample of 1.0BA has a stronger peak intensity than that of pure BiOCl-S, which proves the presence of more $\bullet O_2^-$ and thus its higher oxygen activation ability.

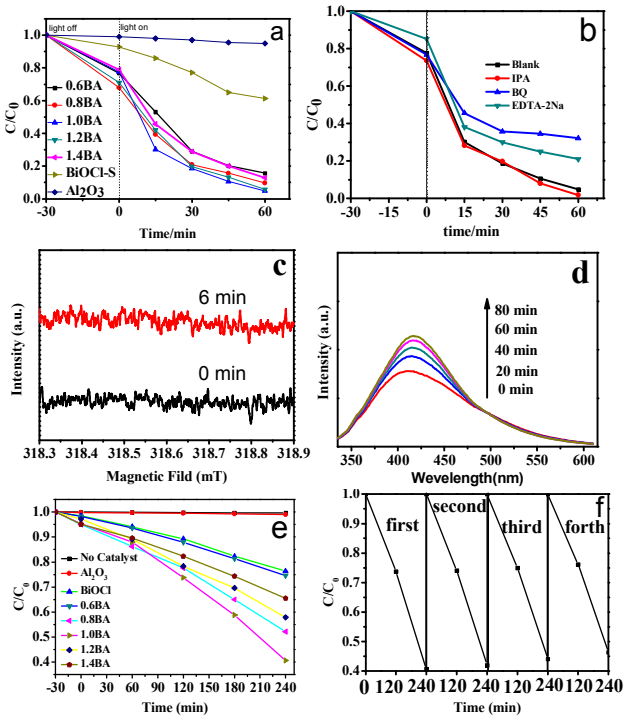

Fig. 8. (a) Photocatalytic degradation of RhB of various samples, (b) the RhB degradation of 1.0BA in the presence of scavengers, (c) the ESR signal of the DMPO-•OH adduct and 1.0BA, (d) the •OH-trapping fluorescence spectra of 1.0BA in the TA solution (excitation at 315 nm, emission at 425 nm) , (e) the photocatalytic activity in degradation of phenol over various samples, and (f) the recycling test of 1.0 BA in degradation of phenol.

Table 2. Pseudo-first-order kinetics for the photocatalytic degradation of RhB for various samples.

Sample	Fitted equation	Reaction rate constant, K (min^{-1})	Correlation coefficient, R
Al_2O_3	y=0.0007x+0.0101	0.0007	0.9981
BiOCl	y=0.0071x+0.0747	0.0071	0.9963
0.6BA	y=0.0282x+0.2640	0.0282	0.9973
0.8BA	y=0.03355x+0.3871	0.0335	0.9981
1.0BA	y=0.0465x+0.2536	0.0465	0.9976
1.2BA	y=0.0403x+0.3425	0.0403	0.9986
1.4BA	y=0.0310x+0.2357	0.0310	0.9989

To thoroughly investigate the reactive species generated in the photocatalytic process, the degradation of RhB in the presence of various scavengers were carried out. As displayed in Fig. 8a, the highest degradation efficiency is reached over the sample 1.0BA. The fitted pseudo-first-order kinetics equation for each sample is listed in Table 2, from which it is seen that 1.0BA has the largest reaction rate constant of 0.0465 min^{-1}, which is approximately 6.55 times that of the pristine BiOCl (0.0071 min^{-1}). Meanwhile, the activity order of all of the photocatalysts is consistent with the NBT degradation results. The result also implies that $\bullet O_2^-$ plays a crucial role in oxidizing RhB. On the other hand, it is also can be seen that the heterojunctions exhibit much higher adsorptive efficiency than both pure Al_2O_3 and BiOCl. To

Table 3. S_{BET}, pore parameters, and Zeta-potentials of the samples.

Sample	S_{BET} (m^2/g)	Average pore diameter (nm)	Total pore volume (cm^3/g)	Zeta-potential (mV)
Al_2O_3	414.50	2.31	0.2396	-21.3
BiOCl	10.31	9.40	0.0242	-31.7
0.6BA	152.44	3.38	0.1288	-38.2
0.8BA	122.07	3.75	0.1146	-36.5
1.0BA	50.71	4.23	0.0537	-45.4
1.2BA	82.39	3.49	0.0719	-46.3
1.4BA	39.87	5.55	0.0554	-45.3

investigate the reason, N_2 adsorption–desorption measurements were conducted. The isotherms and the corresponding pore size distribution curves (inset) of the samples are shown in Fig. S1, and the calculated BET specific surface areas (S_{BET}) and pore parameters are listed in Table 3. Although pure Al_2O_3 exhibits the highest surface area of 414.50 m^2/g, its adsorptive yield for RhB is the lowest. Therefore, surface area is not the decisive factor for RhB adsorption. Considering RhB is a typical cationic dye, we performed Zeta-potential measurement and the results are listed in Table 3. It is seen that all the samples possess surface negative charges and the absolute value of Al_2O_3 is the lowest. This feature may explain the higher and excellent adsorption ability of the heterojunctions and BiOCl than that of Al_2O_3 for cationic RhB. From this result, it can be concluded that surface charge is a more crucial factor than surface area responsible for the adsorption behaviour.

The scavenger experiment results shown in Fig. 8b indicate that there is nearlyno additional decolourization of RhB after the addition of IPA, which acts as a •OH radical scavenger, because the redox potential of $\bullet OH/H_2O$ (+2.27 eV versus the standard hydrogen electrode (SHE))[57] or $\bullet OH/OH^-$ (+1.99 eV)[58] is larger than that of Bi_2O_4/BiO^+ (Bi^V/Bi^{III}) ($E°$ =+1.59 eV),[59] and thus the photo-generated holes cannot react with H_2O or OH^- to form •OH in the case of the Bi-based photocatalyst. The ESR result shown in Fig. 8c indicates that there are no signals for the DMPO-•OH adduct either with or without visible-light irradiation. The TAOH fluorescence signals at different times are shown in Fig. 8d and illustrate that with time there is a very slow enhancement in peak intensity, further indicating that •OH radicals are only slightly induced in the photo-degradation of RhB. It is also observed that both EDTA and BQ can reduce the removal efficiency of RhB, especially BQ, confirming that $\bullet O_2^-$ is the dominant active species responsible for the elimination of RhB; furthermore,photo-induced holes also play a role. The experimental results prove that combining amorphous Al_2O_3 with BiOCl via a one-step combustion route is an effective strategy for improving the oxygen activation performance.

To investigate the photocatalytic activity of the samples excluding the photosensitization of colored organic dyes, the colorless phenol was selected as objective pollutant. The results are shown in Fig. 8e. The blank photocatalytic test shows that the degradation efficiency of 50 mg/L of phenol is only 1% in 240 min in the absence of catalyst, confirming that

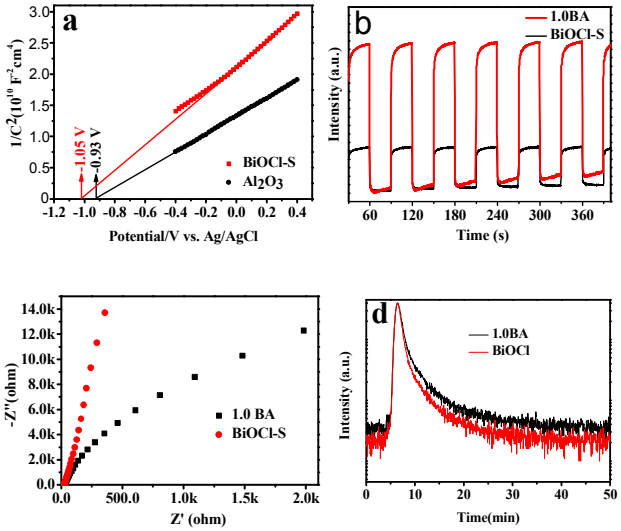

Fig. 9. (a) Mott–Schottky plots, (b) thetransient photocurrent responses with light on-and-off cycles, (c) EIS Nyquist plots, and (d) the time-resolved fluorescence decay spectra of BiOCl-S and the 1.0BA hybrid.

there is almost no self-photolysis of phenol under visible light irradiation. When photocatalysts were introduced to the reaction system, photocatalytic degradation efficiency of phenol is about 25.4%, 47.9%, 60.0%, 42.1%, 34.5%, 23.6%, and 1.3% over 0.6BA, 0.8BA, 1.0BA, 1.2BA, 1.4BA, pure BiOCl-S and pure Al_2O_3, respectively. 1.0BA also exhibits the highest photocatalytic activity among these samples, showing the combination of BiOCl with the as-prepared photo-active Al_2O_3 is an effective route.

To investigate the stability of the photocatalyst which is crucial for practical application, the recycling test of sample 1.0BA in degradation of phenol was conducted repeatedly for four times, as shown in Fig. 8f. The photocatalytic efficiency decreases slightly from 60.0% to 53.6% after four times recycling caused by the loss of photocatalyst particles. The experimental results prove that the sample combining amorphous Al_2O_3 with BiOCl via one-step combustion route is stable.

Electron transfer route and activation mechanism of heterojunctions

To detect the electron transfer route between BiOCl-S and Al_2O_3, a Mott–Schottky measurement was firstly used to compare their energy band positions. The results shown in Fig. 9a clearly illustrate that V_{fb} for the Al_2O_3 electrode is – 0.93 V (versus Ag/AgCl), corresponding to -0.33 V *vs*. RHE, which is lower than the position of BiOCl-S and makes the migration of photo-generated electrons from the CB of BiOCl-S to that of Al_2O_3 possible. Furthermore, the electrons on this position are capable of reacting with O_2 to form $\bullet O_2^-$.[57]

The transient photocurrent curves of pristine BiOCl-S and the 1.0BA composite electrodes are shown in Fig. 9b. It is clear that there is nearly no abatement of thephotocurrent intensity for both of the samples, even after six intermittent on-off cycles, exhibiting their excellent reproducibility and stability. Meanwhile, the photocurrent intensity of the 1.0BA electrode

Table 4. Kinetics parameters for the time-resolved photoluminescence decay curves of the BiOCl-S and 1.0BA samples.

Sample	τ1 (ns)	P1 (%)	τ2 (ns)	P2 (%)
BiOCl-S	0.26	68.08	3.18	31.92
1.0BA	0.37	60.64	3.73	39.36

is nearly 3.7 times that of the pure BiOCl-S electrode, implying a great improvement in the separation efficiency of the photo-generated electron-hole pairs for the heterostructured composite because of the alignment of the energy band structures of the as-prepared BiOCl-S and Al_2O_3.

To further observe theinternal resistances and electronic transport rate of the photocatalysts, EIS measurements were performed. The smaller the arc radius, the higher charge transfer efficiency is.[60] In this case, the arc radius of the 1.0BA sample is smaller than that of BiOCl-S, as shown in Fig. 9c, suggesting that the 1.0BA heterojunction has a resistance that is lower than that of pure BiOCl, which can accelerate the interfacial electron mobility and lead to a higher photocatalytic ability. This observation is consistent with the photocurrent result.

To detect the photophysical characteristics of the photo-induced charge carriers, the time-resolved photoluminescence decay spectra of representative 1.0BA and BiOCl-S were recorded, as shown in Fig. 9d. The decay curves were fitted via a double-exponential model using Eq. (9),[61,62] and the lifetimes and their percentages are listed in Table 4.

$$I(t) = P_1 \exp(-t/\tau_1) + P_2 \exp(-t/\tau_2) \qquad (9)$$

In Eq. (9), I(t) represents the PL signal intensity, τ_1 and τ_2 are the decay times, and P_1 and P_2 are the corresponding percentages. The biexponential model implies that two types of emissive states participated in the PL decay. The fast decay lifetime (τ1) originates from the radiative emission via the direct interband exciton recombination, and the slower lifetime (τ2) is ascribed to the emission decay of the indirect recombination.[61] In this research, three conclusions are drawn from the time-resolved PL spectra. Firstly, the proportion of the short-living component is prolonged from 31.92% in BiOCl-S to 39.36% in 1.0BA, indicating that the indirect recombination of excitons is promoted in the heterojunction because of the existence of the interface. Secondly, both the short lifetime and the long lifetime are increased in the hybrid compared with the single BiOCl, indicating an enhanced charge transfer ability. Thirdly, the corresponding average lifetime (calculated from τP) of 1.0BA is 1.69 ns, which is approximately 1.42 times longer that of BOCl-S (1.19 ns), which quantitatively reveals the probability of the improved mobility of electrons in the heterojunction.

On the basis of the above-discussed analysis and results, a potential route of the electron transfer and oxygen activation

of the $BiOCl/Al_2O_3$ heterojunctions under visible light is proposed in Scheme 2. Firstly, electrons in the valence band of BiOClare excited to the CB upon visible-light irradiation. O_2 adsorbed on the surface of BiOCl with surface oxygen vacanciesare activated to form $\bullet O_2^-$ radicals by reacting with a portionof the excited electrons. Meanwhile, some of the

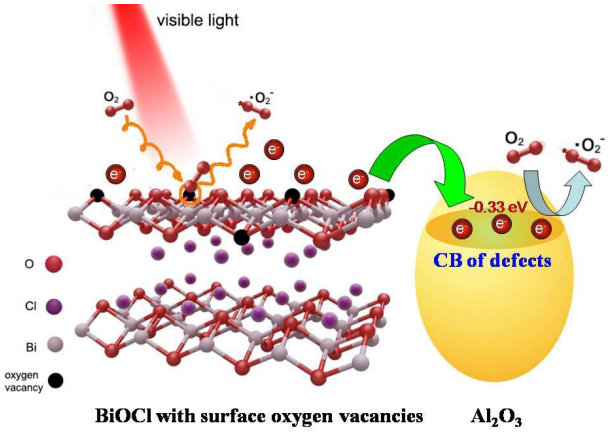

Scheme 2. Proposed transfer route of the photo-generated electrons from BiOCl to Al_2O_3 for activating molecular oxygen under visible-light irradiation.

electrons in the CB of BiOCl move to the CB of the defective Al_2O_3 and then activate O_2 to produce $\bullet O_2^-$ radicals.

Conclusions

$BiOCl/Al_2O_3$ heterojunctionwere successfully obtained for the first time via the self-combustion of ionic liquids in the presence of $(C_2H_5)_2NH{\cdot}HCl$, which not only acts as the cation of the ionic liquid and the fuel but also induces the growth of {001} facetsin BiOCl. Surface oxygen vacancies were constructed by an excess of $(C_2H_5)_2NH{\cdot}HCl$ because of the release of oxygen atoms on the surface of BiOCl. The existence of surface oxygen vacanciesnarrows the energy band gap significantly from 3.15 to 2.72 eV and lifts the position of the conduction band approximately 0.19 V, which are beneficial to the photo-absorption and activation of molecular oxygen, respectively. Based on the formation of BiOCl with surface oxygen vacancies, $BiOCl/Al_2O_3$ heterojunctions were in-situ fabricated in a single step. The $BiOCl/Al_2O_3$ with a molar ratio of 1:1 exhibited the highest oxygen activation and photocatalytic degradation of RhB, which areapproximately 1.80 and 6.55 times that of pristine BiOCl, respectively. The enhanced effect is attributed to the synergistic effects: the effective transfer of electrons from the CB of BiOCl to that of the defective Al_2O_3, the well-contacted interfaces between BiOCl and Al_2O_3 caused by the homogeneous mixing at ionic level in liquid precursor, and theenergy band alignment between BiOCl and Al_2O_3 that is beneficial to activating molecular oxygen. In addition, the CB position of the defective Al_2O_3 is firstly proposed at -0.33 V *vs*. RHE. The proposed CB position of inexpensive Al_2O_3 may broaden its application in the field of photocatalysis as an active material. The present work may provide a new route for constructing nanomaterials with desirable surfaces and facets and deepen the understanding of the function of traditional inert materials in the field of photocatalysis.

Acknowledgements

We are grateful for the financial support from the National Natural Science Foundation of China (21376061, 21076060, 20140654), the Program for New Century Excellent Talents in University (NCET-12-0686), the Natural Science Foundation for Distinguished Young Scholars of Hebei Province (B2015208010), and the Scientific Research Foundation for High-Level Talent in University of Hebei Province (GCC2014057).

Notes and references

1 F. Yang, Y. M. Choi, P. Liu, D. Stacchiola, J. Hrbek and J. A. Rodriguez, *J. Am. Chem. Soc*., 2011, **133**, 11474–11477.
2 D. Jiang, W. Z. Wang, L. Zhang, Y. L. Zheng and Z. Wang, *ACS Catal*., 2015, **5**, 4851–4858.
3 T. A. Baker, B. J. Xu, S. C. Jensen, C. M. Friend and E. Kaxiras, *Cataly. Sci. Technol.*, 2011, **1**, 1166–1174.
4 J. Tian, Y. H. Leng, H. Z. Cui and H. Liu, *J. Hazard. Mater*., 2015, **299**, 165–173.
5 M. Setvín, U. Aschauer, P. Scheiber, Y. F. Li, W. Y. Hou, M. Schmid, A. Selloni and U. Diebold, *Science*, 2013, **341**, 988–991.
6 Q. P. Wu and R.van de Krol, *J. Am. Chem. Soc*., 2012, **134**, 9369–9375.
7 K. Xie, N. Umezawa, N. Zhang, P. Reunchan, Y. J. Zhang and J. H. Ye, *Energy Environ. Sci*., 2011, **4**, 4211–4219.
8 F. T. Li, Q. Wang, J. R. Ran, Y. J. Hao, X. J. Wang, D. S. Zhao and S. Z. Qiao, *Nanoscale*, 2015, **7**, 1116–1126.
9 W. G. Tu, Y. Zhou and Z. G. Zou, *Adv. Mater*., 2014, **26**, 4607–4626.
10 M. L. Guan, C. Xiao, J. Zhang, S. J. Fan, R. An, Q. M. Cheng, J. F. Xie, M. Zhou, B. J. Ye and Y. Xie, *J. Am. Chem. Soc*., **2013**, 135, 10411–10417.
11 S. J. A. Moniz, S. A. Shevlin, D. J. Martin, Z. X. Guo and J. W. Tang, *Energy Environ. Sci*., 2015, **8**, 731–759.
12 W. L. Yang, L. Zhang, Y. Hu, Y. J. Zhong, H. B. Wu and X. W. Lou, *Angew. Chem., Int. Ed.*, 2012, **51**, 11501–11504.
13 J. R. Ran, J. Zhang, J. G. Yu, M. Jaroniec and S. Z. Qiao, *Chem. Soc. Rev*., 2014, **43**, 7787–7812.
14 S. Z. Chu, S. Inoue, K. Wada, D. Li and H. Haneda, *J. Mater. Chem*., 2003, **13**, 866–870.
15 H. Choi, E. Stathatos and D. D. Dionysiou, *Appl. Catal. B*, 2006, **63**, 60–67.
16 X. B. Ke, X. G. Zhang, J. Zhao, S. Sarina, J. Barry and H. Y. Zhu, *Green Chem*., 2013, **15**, 236–244.
17 M. Bouslama, M. C. Amamra, Z. Jia, M. B. Amar, K. Chhor, O. Brinza, M. Abderrabba, J. L. Vignes and A. Kanaev, *ACS Catal*., 2012, **2**, 1884–1892.
18 D. H. Xia, L. L. Hu, C. He, W. Q. Pan, T. S. Yang, Y. C. Yang and D. Shu, *Chem. Eng. J.*, 2015, **279**, 929–938.
19 P. P. Hankare, R. P. Patil, A. Jadhav, K. M. Garadkar and R. Sasikala, *Appl. Catal. B*, 2011, **107**, 333–339.
20 F. T. Li, Y. Zhao, Y. J. Hao, X. J. Wang, R. H. Liu, D. S. Zhao and D. M. Chen, *J. Hazard. Mater*., 2012, **239–240**, 118–127.
21 F. T. Li, Y. Zhao, Y. Liu, Y. J. Hao, R. H. Liu and D. S. Zhao, *Chem. Eng. J.*, 2011, **173**, 750–759.

22 M. Ishimaru, Y. Hirotsu, I. V. Afanasyev-Charkin and K. E. Sickafus, *J. Phys.: Condens. Matter*, 2002, **14**, 1237–1247.
23 F. T. Li, S. J. Liu, Y. B. Xue, X. J. Wang, Y. J. Hao, J. Zhao, R. H. Liu and D.S. Zhao, *Chem. –Eur. J.*, 2015, **21**, 10149–10159.
24 F. T. Li, Y. Zhao, Q. Wang, X. J. Wang, Y. J. Hao, R. H. Liu and D. S. Zhao, *J. Hazard. Mater.*, 2015, **283**, 371–381.
25 F. T. Li, Y. B. Xue, B. Li, Y. J. Hao, X. J. Wang, R. H. Liu and J. Zhao, *Ind. Eng. Chem. Res*. 2014, **53**, 19540−19549.
26 M. Polat, A. M. Soylu, D. A. Erdogan, H. Erguven, E. I. Vovk and E. Ozensoy, *Catal. Today*, 2015, **241**, 25−32.
27 A. A. Ismail, I. Abdelfattah, M. F. Atitar, L. Robben, H. Bouzid, S. A. Al-Sayari and D. W. Bahnemann, *Sep. Purif. Technol*., 2015, **145**, 147−153.
28 H. T. Tian, J. W. Li, M. Ge, Y. P. Zhao and L. Li, *Cataly. Sci. Technol.*, 2012, **2**, 2351–2355.
29 X. Liu, H. M. Yang, H. Y. Dai, X. M. Mao and Z. H. Liang, *Green Chem*., 2015, **17**, 199–203.
30 J. Jiang, K. Zhao, X. Y. Xiao and L. Z. Zhang, *J. Am. Chem. Soc*., 2012, **134**, 4473–4476.
31 W. Y. Su, J. Wang, Y. X. Huang, W. J. Wang, L. Wu, X. X. Wang and P. Liu, *Scripta Mater*., 2010, **62**, 345–348.
32 L. Q. Ye, X. L. Jin, Y. M. Leng, Y. R. Su, H. Q. Xie and C. Liu, *J. Power Sources*, 2015, **293**, 409–415.
33 K. Zhao, L. Z. Zhang, J. J. Wang, Q. X. Li, W. W. He and J. J. Yin, *J. Am. Chem. Soc*., 2013, **135**, 15750−15753.
34 Y. Yu, C. Y. Cao, H. Liu, P. Li, F. F. Wei, Y. Jiang and W. G. Song, *J. Mater. Chem. A*, 2014, 2, 1677−1681.
35 H. Li, J. G. Shi, K. Zhao and L. Z. Zhang, *Nanoscale*, 2014, **6**, 14168−14173.
36 J. Di, J. X. Xia, M. X. Ji, B. Wang, S. Yin, Q. Zhang, Z. G. Chen and H. M. Li, *ACS Appl. Mater. Interfaces,* 2015, **7**, 20111–20123.
37 F. T. Li, Y. Liu, Z. M. Sun, Y. Zhao, R. H. Liu, L. J. Chen and D. S. Zhao, *Cataly. Sci. Technol.*, 2012, **2**, 1455–1462.
38 F. T. Li, J. R. Ran, M. Jaroniec and S. Z. Qiao, *Nanoscale*, 2015, **7**, 17590–17610.
39 F. T. Li, Q. Wang, X. J. Wang, B. Li, Y. J. Hao, R. H. Liu and D. S. Zhao, *Appl. Catal. B*, 2014, **150–151**, 574–584.
40 B. H. J. Bielski, G. G. Shiue and S. Bajuk, *J. Phys. Chem*., 1980, **84**, 830–833.
41 M. Quinones, Y. Zhang, P. Riascos, H. M. Hwang, W. G. Aker, X. He and R.M. Gao, *Photochem. Photobiol.*, 2014, **90**, 374–379.
42 K. I. Ishibashi, A. Fujishima, T. Watanabe and K. Hashimoto, *Electrochem. Commun*., 2000, **2**, 207–210.
43 Q. Xiao, Z. C. Si, J. Zhang, C. Xiao and X. K. Tan, *J. Hazard. Mater*., 2008, **150**, 62–67.
44 Y. X. Chen, S. Y. Yang, K. Wang and L. P. Lou, *J. Photoch. Photobio. A,* 2005, **172**, 47–54..
45 M. C. Yin, Z. S. Li, J. H. Kou and Z. G. Zou, *Environ. Sci. Technol.*, 2009, **43**, 8361−8366.
46 Y. F. Liu, W. Q. Yao, D. Liu, R. L. Zong, M. Zhang, X. G. Ma and Y. F. Zhu, *Appl. Catal. B*, 2015, **163**, 547–553.
47 L. Q. Ye, J. Y. Liu, Z. Jiang, T. Y. Peng and L. Zan, *Appl. Catal. B*, 2013, **142–143**, 1–7.
48 A. Dandapat, H. Gnayem and Y. Sasson, *Chem. Commun*., 2016, **52**, 2161–2164.
49 S. R. Jain, K. C. Adiga and V. R. P. Verneker, *Combus. Flame*, 1981, **40**, 71–79.
50 M. J. Chai, X. M. Chen, Y. Zhao, R. H. Liu, J. Zhao and F. T. Li, Chem. Lett., 2014, **43**, 1743–1745.
51 D. Malwal and P. Gopinath, *Cataly. Sci. Technol.*, 2016, **6**, 4458–4472.
52 Z. Wang, C. Y. Yang, T. Q. Lin, H. Yin, P. Chen, D. Y. Wan, F. F. Xu, F. Q. Huang, J. H. Lin, X. M. Xie and M. H. Jiang, *Energy Environ. Sci*. 2013, **6**, 3007–3014.
53 P. Hajra , S. Shyamal , A. Bera , H. Mandal , D. Sariket , M. Kundu, S. Pande and C. Bhattachary, *Electrochim. Acta*, 2015, **185**, 229–235.
54 Y. Hou, F. Zuo, A. Dagg and P. Y. Feng, *Angew. Chem., Int. Ed*., 2013, **52**, 1248 –1252.
55 S. J. Hong, S. Lee, J. S. Jang and J. S. Lee, *Energy Environ. Sci*. 2011, **4**, 1781–1787.
56 M. Zhang, X. J. Bai, D. Liu, J. Wang and Y. F. Zhu, *Appl. Catal. B*, 2015, **164**, 77–81.
57 A. Fujishima and X. T. Zhang, *C. R. Chimie*, 2006, **9**, 750−760.
58 S. Kim and W. Choi, *Environ. Sci. Technol.*, 2002, 36, 2019−2025.
59 R. C. Weast, Handbook of Chemistry and Physics. CRC Press: Boca Raton, FL, 1988.
60 M. M. Khan, S. A. Ansari, D. Pradhan, M. O. Ansari, D. H. Han, J. Lee and M. H. Cho, *J. Mater. Chem. A*, 2014, **2**, 637−644.
61 H. Li, J. Shang, Z. H. Ai and L. Z. Zhang, *J. Am. Chem. Soc*., 2015, **137**, 6393−6399.
62 M. V. Dozzi, C. D'Andrea, B. Ohtani, G. Valentini, E. Selli, *J. Phys. Chem. C*, 2013, **117**, 25586−25595.

The conduction band position of defective Al_2O_3 obtained via combustion synthesis is proposed and the in-situ as-prepared heterojunctions containing Al_2O_3 and {001} facets-exposed BiOCl with surface oxygen vacancies exhibit excellent performance for molecular oxygen activation.